Origin of active sites on silica-magnesia catalysts and control of reactive environment in the one-step ethanol-to-butadiene process

Sang-Ho Chung
Utrecht University https://orcid.org/0000-0002-7647-2237
Teng Li
KAUST
Tuiana Shoinkhorova
King Abdullah University of Science and Technology
Adrian Ramirez
KAUST
Ildar Mukhambetov
KAUST
Edy Abou-Hamad
King Abdullah University of Science and Technology (KAUST)
Genrikh Shterk
KAUST
Selvedin Telalovic
KAUST
Alla Dikhtiarenko
King Abdullah University of Science and Technology https://orcid.org/0000-0002-3372-2435
Bart Sirks
Utrecht University
Polina Lavrik
KAUST https://orcid.org/0000-0002-9305-5363
Xinqi Tang
KAUST Corelabs
Bert Weckhuysen
Utrecht University https://orcid.org/0000-0001-5245-1426
Pieter Bruijnincx
Inorganic Chemistry and Catalysis, Debye Institute for Nanomaterials Science, Utrecht University
Jorge Gascon
King Abdullah University of Science and Technology https://orcid.org/0000-0001-7558-7123
Javier Ruiz-Martinez (javier.ruizmartinez@kaust.edu.sa)

KAUST

Article

Keywords:

Posted Date: May 18th, 2022

DOI: https://doi.org/10.21203/rs.3.rs-1581970/v1

Origin of active sites on silica–magnesia catalysts and control of reactive environment in the one-step ethanol-to-butadiene process

Sang–Ho Chung[1]*, Teng Li[1], Tuiana Shoinkhorova[1], Adrian Ramirez[1], Ildar Mukhambetov[1], Edy Abdou–Hamad[2], Genrikh Shterk[1], Selvedin Telalovic[1], Alla Dikhtiarenko[1], Bart Sirks[3], Polina Lavrik[1], Xinqi Tang[2], Bert M. Weckhuysen[3], Pieter C.A. Bruijnicx[3,4], Jorge Gascon[1], and Javier Ruiz–Martinez[1]*

[1]King Abdullah University of Science and Technology, KAUST Catalysis Center (KCC), Thuwal 23955, Saudi Arabia.

*e–mail: sangho.chung@kaust.edu.sa, javier.ruizmartinez@kaust.edu.sa

[2]King Abdullah University of Science and Technology, Core Labs, Thuwal 23955, Saudi Arabia.

[3]Inorganic Chemistry and Catalysis Group, Debye Institute for Nanomaterials Science, Utrecht University, Universiteitsweg 99, 3584 CG Utrecht, The Netherlands.

[4]Organic Chemistry and Catalysis Group, Debye Institute for Nanomaterials Science, Utrecht University, Universiteitsweg 99, 3584 CG Utrecht, The Netherlands.

Wet-kneaded silica–magnesia is a benchmark catalyst for the one–step ethanol-to-butadiene Lebedev process. Magnesium silicates, formed during wet-kneading, have been proposed as active sites responsible for butadiene formation, and their catalytic performance has been mainly explained by the variations in the ratio of acid and base sites. While the Lebedev process was developed in the 1930s, However, a detailed insight into how the peculiar, yet essential wet-kneading synthesis leads to the generation, location, and catalytic role of magnesium silicates has not been fully established. Here, we demonstrate that magnesium silicates formation occurs *via* dissolution of Si and Mg subunits from SiO_2 and $Mg(OH)_2$ precursors, initiated by the alkaline pH of the aqueous wet-kneading medium, followed by cross-deposition of the dissolved species on the precursor surfaces. Building on these new insights, two individual model systems (Mg/SiO_2 and Si/MgO) were synthesized, representative of the constituents of the wet-kneaded silica–magnesia catalyst, by selective dissolution/deposition induced by pH alteration of the aqueous wet-kneading medium. Using these model catalysts, we demonstrate that the location of the magnesium silicates (*i.e.*, Mg on SiO_2 or Si on MgO) governs not only their chemical nature but also the ethanol adsorption configuration, which ultimately cause the catalyst material to be selective mainly for ethylene or butadiene. We demonstrate close proximity at the particle level of the of acid and basic sites is a prerequisite to promote the butadiene formation. The insights gained from the new structure–performance relationships that correlate catalytic activity with types and nature of

magnesium silicates can offer new possibilities for the development of next generation Lebedev catalysts.

1,3–Butadiene (butadiene) is a key monomer in the polymer industry. It is used for various end–products including poly–butadiene–rubber (PBR), styrene–butadiene–rubber (SBR) and acrylonitrile–butadiene–rubber (ABR).[1,2] Currently, butadiene is mainly produced as a byproduct of the naphtha steam cracking unit, which is designed for ethylene/propylene production. Correspondingly, the price of butadiene fluctuates with the supply–demand chain for ethylene.[3] This issue is exacerbated by the exploitation of shale gas, which leads to shortages in the butadiene supply.[1,4,5] Moreover, these routes are fossil-based and clearly not sustainable. The development of alternative and more sustainable production process for butadiene is needed. The Lebedev process, a process developed in the 1930s that converts ethanol to butadiene in a single catalytic reactor, is thus again receiving much attention, as part of the value chain of both bioethanol production[2,3,5–8] as well as the more recent, cutting–edge processes that convert CO_2–to–ethanol.[9–11]

Silica–magnesia has been a benchmark catalyst in the Lebedev process, owing to its originality in the industrial process in the 1940s and its stable catalytic performance.[12] The preparation method of silica–magnesia catalyst considerably influences its catalytic performance, and among the methods studied, wet-kneading yields the most active catalyst.[3,13] This superior performance has been attributed to the formation of distinct magnesium silicates.[14–16] Wet-kneading typically utilizes solid precursors (*e.g.*, SiO_2 and $Mg(OH)_2$) in water with continuous mixing (Fig. 1a).[17] Various research efforts have aimed at achieving higher butadiene yields by optimizing the synthesis procedure of wet-kneaded silica–magnesia catalysts. Several synthesis parameters, such as the types of Si[18] and Mg precursors,[17] the precursor morphology,[19] and the Si/Mg ratio have been investigated.[17,20] Post-synthesis parameters, such as calcination, have also been shown to important, as these alter the chemical structure of the formed magnesium silicates, and therefore, the catalytic performance.[21] In any case, all studies conclude that the optimal catalyst for the Lebedev process must strike a delicate balance between acidic and base sites.[8,13–15,17,18,21–24]

Even after more than 70 years, however, the fundamental details of how wet-kneading generates the active sites for butadiene formation and corresponding silica–magnesia phases have not been fully elucidated. Studies have commonly considered the catalytic sites of wet-kneaded silica–magnesia for the Lebedev process as a combination of different oxide forms (bulk silica, magnesia and "magnesium silicate species" (Mg–O–Si)) and their surface hydroxyl groups.[16,25] However, the origin, location and nature of the "active species" in the Lebedev process are still open questions.

Here we provide new, detailed insight into the genesis, location and nature of catalytically active sites of wet-kneaded silica–magnesia catalyst for the Lebedev process. By varying the duration of wet-kneading, we show how the pertinent magnesium silicates are formed from their Si and Mg precursors. Based on this, the traditional wet-kneading conditions were modified by altering the pH of the wet-kneading medium, to selectively prepare the individual constituents of the wet-kneaded silica–magnesia catalyst, *i.e.*, Mg-decorated SiO_2 and Si-decorated MgO (Mg/SiO_2 and Si/MgO). Following this approach, we discovered that butadiene formation is optimal when acidic sites are surrounded and in close proximity to basic sites at the single–particle level, while minimizing ethylene formation.

Results and discussion

Catalyst synthesis via wet-kneading. The wet-kneaded silica–magnesia catalysts were prepared using spherical Stöber SiO_2 and platelet–shaped $Mg(OH)_2$ at the nominal molar Si/Mg ratio of 1.0, according to synthesis conditions previously optimized for high butadiene yield.[17,21] To better understand wet-kneading, we monitored the pH of the wet-kneading solution *in situ*. Figure 1b shows the pH variation of wet-kneading aqueous medium over 72 h. The sharp, initial increase in pH to 10.4 (*i.e.*, in first 2 min) is owing to the dissolution of brucite ($Mg(OH)_2 \rightarrow Mg^{2+} + 2OH^-$), which initiated the wet-kneading. The pH of the wet-kneading solution then gradually decreased to 9.2, and stabilizes after 10 h of wet-kneading. Elemental analysis by inductively coupled plasma optical emission spectrometry (ICP–OES) showed the molar ratio of Si and Mg in solution to follow the same trend as the pH (exponential decay over wet-kneading time), while the ratio in solid to remain consistent at various synthesis times (Fig. 1c,d). This suggests that the increased amount of hydroxide ions at the initial stage of the wet-kneading process triggers the dissolution of surface Si species of SiO_2, which subsequently redeposit and form magnesium silicate composites.[26]

Even though the rapid pH variation occurs only once at the onset of the process (Fig. 1b, inset), we have observed that wet-kneading is a dynamic process and the reaction still proceeds when the pH has plateaued. Specifically, not only Si but also Mg species continuously dissolve out from $Mg(OH)_2$, as confirmed by elemental analysis (Supplementary Figs. 1,2 and Supplementary Note 1). The dissolved Si and Mg subunits can precipitate on the surfaces of $Mg(OH)_2$ and SiO_2, respectively, as a results of the opposite surface charges in this pH range (cross-deposition).[17] Interestingly, the effect of longer–term wet-kneading (*i.e.*, how dynamic the wet-kneading process is) can be inferred from studies on cement and concrete where changes in similar systems (hydrated magnesium–silicate materials) have been investigated on timescales of a year.[27–29] For example, Roosz et al. conducted the long-term synthesis of $MgO–SiO_2–H_2O$ system for one year and obtained materials containing poorly crystalline magnesium silicates without pristine phases of SiO_2 and MgO.[30] This result suggests the dissolution/deposition of Si and Mg continuously occurred throughout the experiments.

Further insight into the wet-kneading process was obtained *in situ* using solid-state ^{29}Si nuclear magnetic resonance (NMR) spectroscopy (Fig. 1d). As wet-kneading starts immediately after mixing SiO_2 and $Mg(OH)_2$ in water (Fig. 1b), the ^{29}Si NMR spectrum of the physical mixture of SiO_2 and $Mg(OH)_2$ without water is denoted as t = 0. The ^{29}Si NMR spectrum at t = 0 showed three signals at −110, −100 and −91 ppm, which are attributed to siloxane groups (Q^4, $(SiO)_4–Si$), simple silanol (Q^3, $(SiO)_3–Si–OH$), and geminal silanol (Q^2, $(SiO)_2–Si–(OH)_2$), respectively.[31,32] Upon wet-kneading, the Q^4 resonance continuously decreased and the Q^2 and Q^3 resonances gradually became broader. In addition, new features appeared in the downfield shift region from −60 to −90 ppm (*vide infra*). This is in line with the notion above that the wet-kneading method evolves to a pseudosteady state in which not only dissolution of Si species from SiO_2 nanoparticles (for Mg, see below) but also the subsequent formation of new magnesium silicate species is continuous

(Supplementary Fig. 3 and Supplementary Table 1). Note that, in our study, the siloxane signal is still the most prominent after 72 h of wet-kneading, showing that most of the bulk SiO_2 is unreacted. Powder X-ray diffraction (PXRD) patterns of wet-kneaded silica–magnesia catalysts also show that the bulk structure of the SiO_2 and $Mg(OH)_2$ precursors is present (Supplementary Fig. 4).

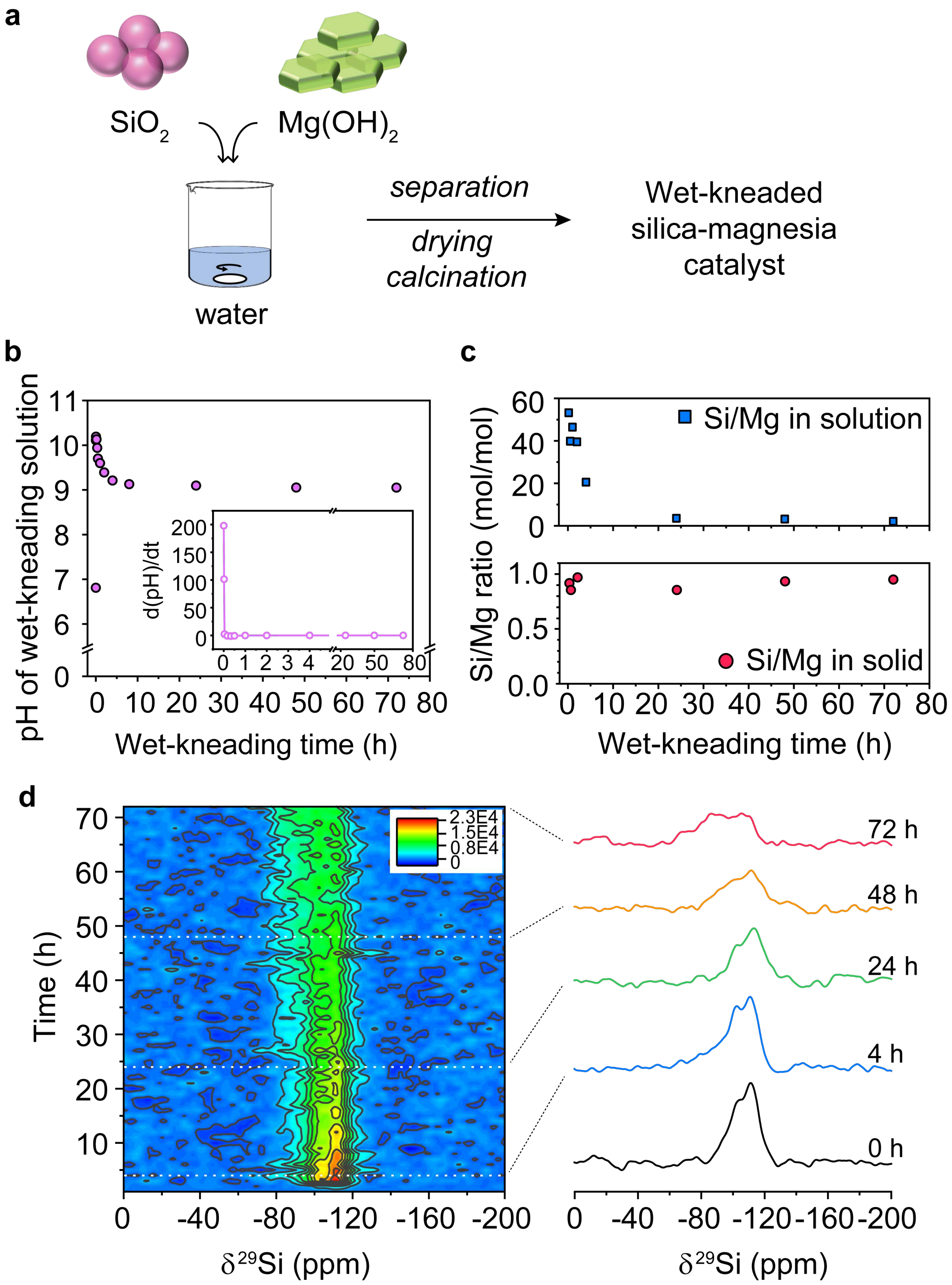

Figure 1 │ Scheme of wet-kneading and time-resolved characterization during wet-kneading. a, Illustration to prepare wet-kneaded silica–magnesia catalyst from spherical silica (SiO_2) and platelet shaped magnesium hydroxide ($Mg(OH)_2$). **b,** pH variation of the wet-kneading solution for 72 h. **c,** Molar ratio of Si and Mg in the wet-kneading solution and the resulting solids determined by ICP–OES. **d,** *In situ* ^{29}Si direct–excitation NMR spectra of a silica-magnesia sample during 72 h of wet-kneading.

To investigate the deposited Si and Mg species at nanoscale, high–angular annular dark–field scanning transmission electron microscopy imaging (HAADF–STEM) with energy dispersive X-ray spectrometry (EDX) analyses were used to characterize a silica–magnesia catalyst isolated after 10 min of wet-kneading (WK–10min–dried, Fig. 2a–e). The precursor SiO_2 and $Mg(OH)_2$ particles are well mixed and in close contact (Fig. 2a,b), which was reported to be beneficial for the Lebedev process owing to intimate interactions of the two components.[17] The high magnification STEM–EDX images of WK–10min–dried show that isolated Si clusters are deposited on the surface of $Mg(OH)_2$ (Fig. 2c,d). This is further confirmed by EDX area profile, clearly showing surface deposition of Si on $Mg(OH)_2$ (Fig. 2e), which is in line with a result of silicon–rich surfaces on wet-kneaded silica–magnesia catalyst by low–energy ion scattering analysis.[25] While not as evident as the Si deposition on $Mg(OH)_2$, Mg species are also found on the SiO_2 domains (Supplementary Fig. 5), indicating deposition of dissolved Mg subunits on the SiO_2. The decreased crystallinity of $Mg(OH)_2$ observed after wet-kneading by PXRD also suggests that the dissolution of Mg subunits from brucite layers with the occurrence of cross-deposition of Si subunits (Supplementary Fig. 4b and Supplementary Table 2).

A detailed chemical characterization of surface Si species on dried catalysts was performed using NMR spectroscopy. Due to the low signal of the surface Si species, dynamic nuclear polarization surface enhanced NMR spectroscopy (DNP–SENS) was applied as it is a powerful and surface–sensitive technique for chemical structure identification.[33] Fig. 2f shows the DNP–enhanced ^{1}H–^{29}Si CP–MAS NMR spectra of pristine SiO_2 and wet-kneaded silica–magnesia samples at two wet-kneading times (10 min and 48 h) after drying. Notably, a distinct ^{29}Si NMR resonance is observed at –66 ppm after wet-kneading. The ^{29}Si NMR isotropic chemical shifts in silicates are related to the degree of anion condensation and the number of neighboring silicon–oxygen tetrahedra.[34–36] We attribute this band to surface silicon species surrounded by magnesium cations (individual Q^0 supported on $Mg(OH)_2$), similar to the Q^0 silicate observed in tricalcium silicate.[36] The formation of dimeric and trimeric Si species (at approximately –77 and –84 ppm, respectively) was also observed especially for the shortly wet-kneaded sample (WK–10min–dried). After 48 h of wet-kneading, the silicate units on brucite have progressively grown into longer silicate chains (oligomeric silicate species), showing upfield ^{29}Si signals higher than –86 ppm (Fig. 2f, inset).[36] The decrease of Q^3/Q^4 intensity ratio upon wet-kneading (from 1.85 to 1.70) indicates that silanol groups are consumed, which can be related to the formation of surface magnesium silicates. Additionally, the resonance at –100 ppm was shifted downfield by ~1 ppm after wet-kneading, indicating overlap of silica Q^3 species (–100 ppm) with the newly formed magnesium silicates (*e.g.*, talc (–98 ppm)[37] and lizardite (–94 ppm)[38]).

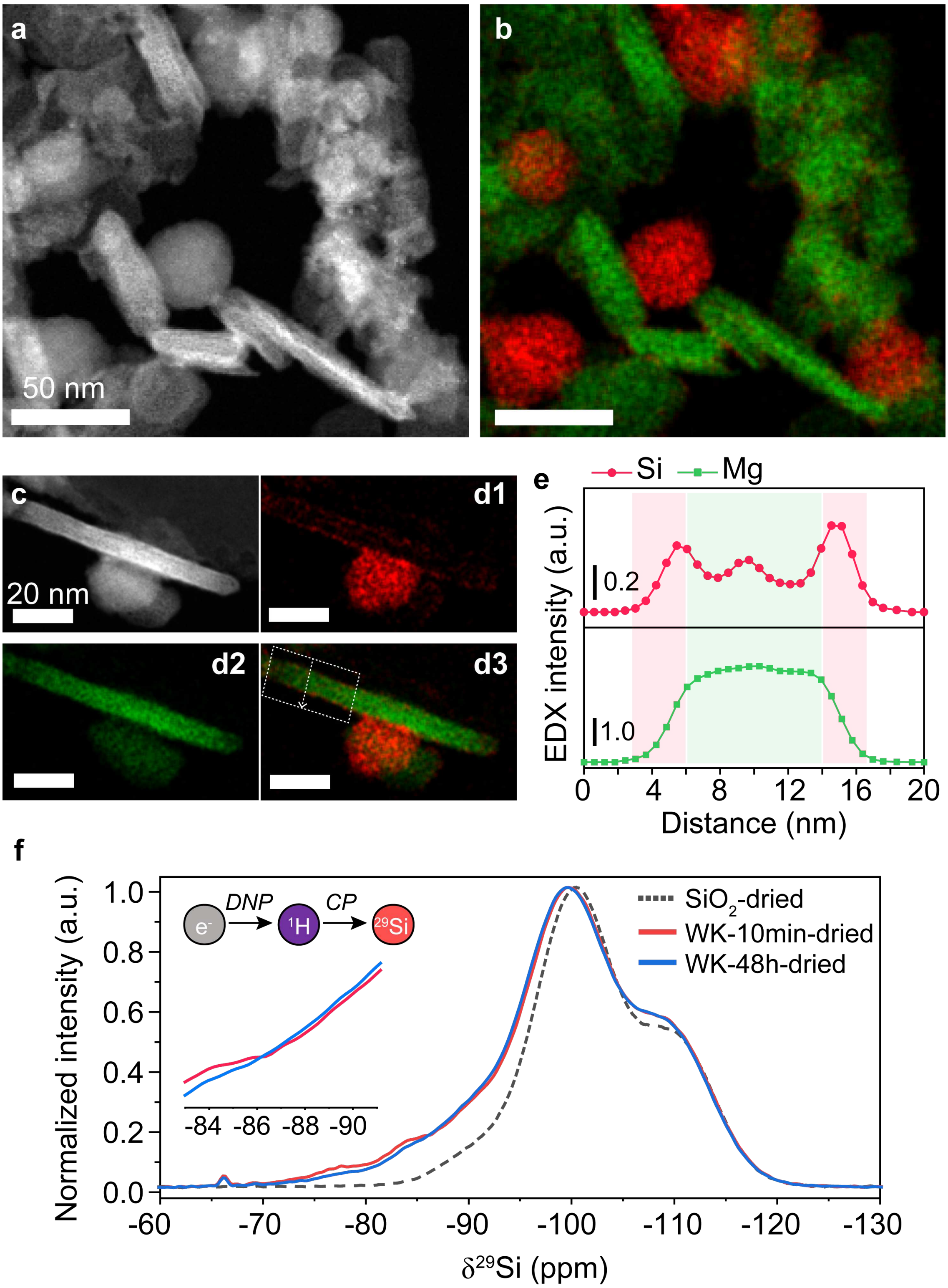

Figure 2 │ Location and type of magnesium silicates on wet-kneaded, dried catalysts drying. a, HAADF–STEM image, **b,** corresponding STEM–EDX elemental maps and **c, d,** magnified STEM–EDX maps of WK–10min–dried catalysts (Si and Mg in red and green, respectively). **e,** EDX area profiles of Si and Mg along the area shown in d3, **f,** DNP–SENS ^{1}H–^{29}Si CP MAS NMR results of pristine SiO_2 and two wet-kneaded silica–magnesia catalysts (WK–10min–dried and WK–48h–dried) after drying.

Effect of thermal treatment. Catalyst calcination is a prerequisite to convert the as-prepared (dried) material into an activated catalyst. We calcined WK–10min–dried catalyst at 500°C for 5 h, a condition optimized to obtain high butadiene yields.[21] Figs. 3a and b show the morphological differences of the wet-kneaded silica-magnesia catalyst before and after calcination. After calcination, the MgO surfaces became substantially corrugated with nanopatterns having ~3 nm intervals between motifs (Supplementary Fig. 6). These patterns are not observed for the physical mixture sample (pristine SiO_2 and $Mg(OH)_2$) after calcination (Supplementary Fig. 7), suggesting that the final morphology of the MgO phase is largely influenced by the Si species deposited on $Mg(OH)_2$ during wet-kneading.

Thermal gravimetric analysis (TGA) of samples provided further insight into the chemistry of the surface hydroxyl groups. Herein, TGA of the dried samples (pristine SiO_2 and $Mg(OH)_2$, and wet-kneaded silica–magnesia) exhibited two distinct mass losses, associated with (i) removal of physisorbed water at approximately 100°C and (ii) surface dehydroxylation of silica and/or magnesium hydroxide at 300°C – 400°C (Fig. 3c and Supplementary Fig. 8).[39] The amount of physisorbed water for the dried SiO_2 is higher than that for the dried $Mg(OH)_2$ (7.1% and 1.9%, respectively), which explains why the actual ratios of Si/Mg in the wet-kneaded silica–magnesia samples are slightly less than 1.0 (0.91 by ICP–OES, Fig.1c). Notably, modification of the $Mg(OH)_2$ surface with Si species considerably hindered the dehydroxylation of $Mg(OH)_2$, shifting the onset and offset temperatures by ~40°C. The phase transformation from $Mg(OH)_2$ to the dehydroxylated MgO periclase phase starts at the external surface layers of the particles[40,41] and is influenced by the substitutional atoms on the $Mg(OH)_2$ surface.[42] We expect that the smaller Si^{4+} ions (r_{ion} for Si^{4+} and Mg^{2+} = 0.026 and 0.072 nm,[43] respectively) that were observed on WK–10min–dried as Si subunits on the surface of $Mg(OH)_2$ (Fig. 2) retarded the surface dehydroxylation of $Mg(OH)_2$,[44,45] creating the corrugated surface structures observed using electron microscopy (Fig. 3b and Supplementary Fig. 7).

Figure 3d shows ^{1}H–^{29}Si CP MAS NMR spectra of wet-kneaded silica–magnesia catalysts before and after calcination. Numerous types of magnesium silicates are found in nature[46] and show distinct ^{29}Si NMR signals reflecting the local silicon environments (Supplementary Fig. 3).[34,47] For example, phyllosilicates, pyroxenes and olivines show characteristic features at approximately −85 to −100 ppm,[17,38,48,49] −75 to −90 ppm[34,47] and −60 to −75 ppm,[48,50,51] respectively. Amorphous magnesium silicates also exhibit ^{29}Si NMR features over wide ranges, *i.e.*, from −70 to −95 ppm.[48,50,52–54] In the wet-kneaded samples, the resonance at −77 ppm is considerably enhanced after calcination, indicating that the proton density around the ^{29}Si nucleus of this magnesium silicate is rather high.[21] We assign this feature to the isolated ^{29}Si species in the MgO domain, which contains hydroxyl groups near the silicon species, to compensate the negatively charged oxygens induced by the incorporation of Si^{4+} in the periclase phase (Mg^{2+}–O^{2-}). The resonances at −84, −93 and −97 ppm are contributions from enstatite,[17,48,50] and lizardite-[38,39] and talc-type phyllosilicates[17,48], respectively.

The chemistry of the Mg species was also directly investigated by ^{25}Mg NMR. Unlike ^{29}Si NMR, the number of ^{25}Mg NMR studies performed on magnesium silicates is rather limited, owing to the intrinsic insensitivity (0.26% to ^{1}H) and relatively low natural abundance (10%) of ^{25}Mg.[38,55,56] Combined with its quadrupolar nature (I = 5/2) with low Larmor frequency (6% to ^{1}H), the acquisition and interpretation of ^{25}Mg NMR spectra is indeed complex. Recent advances in solid–state NMR spectroscopy such as the availability of higher magnetic fields and the use of signal–enhancement pulse sequences offer new opportunities for ^{25}Mg NMR studies.[56] This prompted us to consider natural abundance solid–state ^{25}Mg NMR spectroscopy at high magnetic fields (21.1 T) as a tool for understanding the wet-kneaded silica–magnesia catalysts. The one-dimensional (1D) ^{25}Mg NMR spectra are shown in Fig. 3e and Supplementary Fig. 9. The Mg sites in pristine MgO are highly symmetric (cubic symmetry, Fm–3m)[57], showing a single and symmetrical resonance at 26.3 ppm. After wet-kneading, the ^{25}Mg signals of the silica–magnesia catalysts shifted slightly upfield with asymmetrical broadening, indicating the possible formation of new Mg sites in the wet-kneaded silica-magnesia catalysts. We performed natural abundance ^{25}Mg triple quantum (3Q) MAS experiments for MgO and WK–48–calc (Fig. 3f, Supplementary Fig. 10 and Supplementary Table 3). While pristine MgO showed a symmetrical ^{25}Mg environment (δ_{iso} = 26.3 ppm), the WK–48h–calc catalyst exhibited an asymmetrically broadened feature with relatively large quadrupole coupling constant (C_q = 1.3 MHz), next to the symmetrical signal from MgO. We attribute the broad ^{25}Mg feature of the WK–48h–calc catalyst to structurally disordered Mg species,[58–60] induced by incorporating Si^{4+} in the MgO periclase, *i.e.*, the deviations of the site symmetry from the MgO octahedral structure.

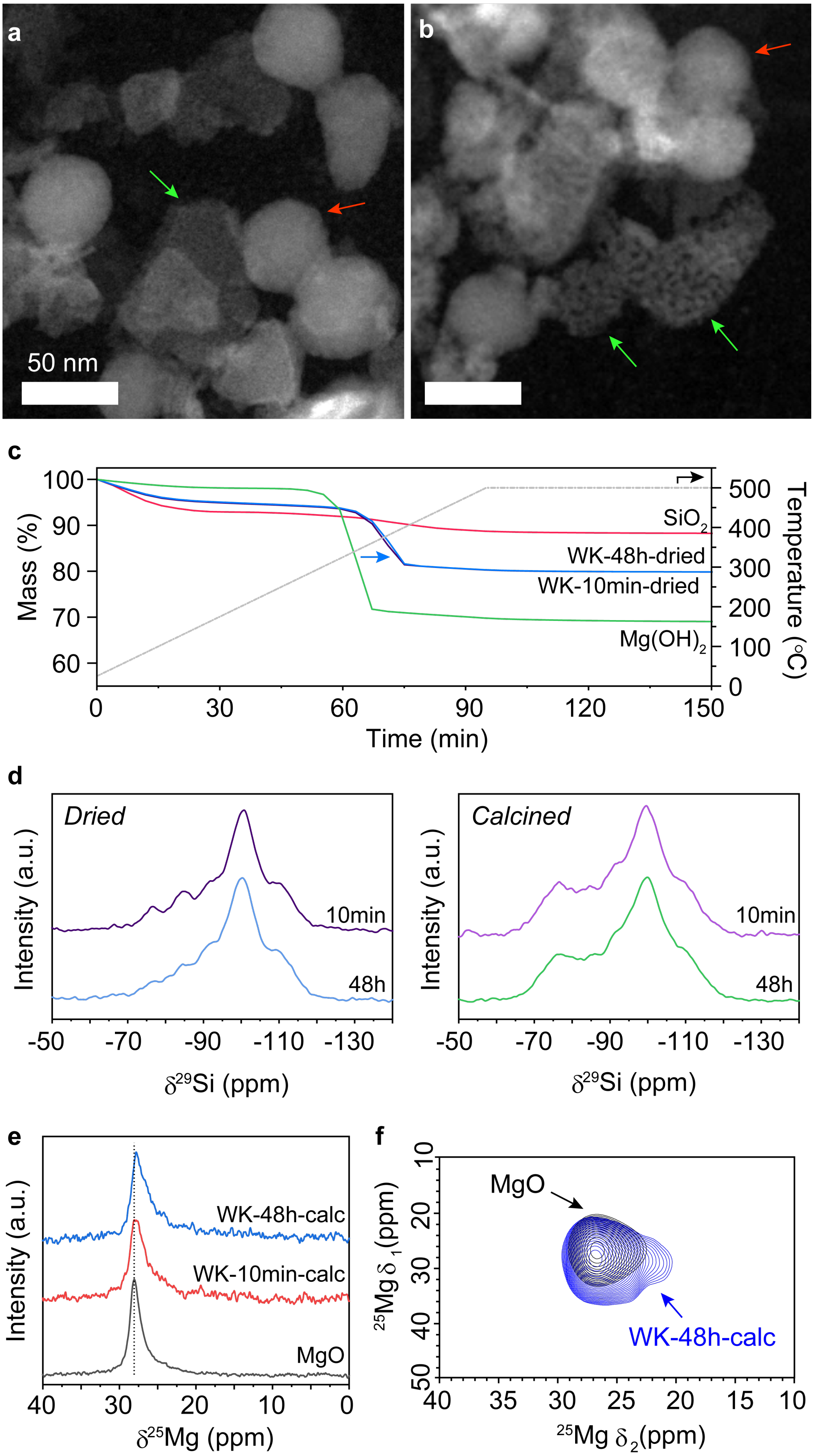

Figure 3 │ Characterization of wet-kneaded silica–magnesia catalysts before and after calcination. HAADF–STEM image of **a**, WK–10min–dried and **b,** WK–10min–calc. SiO_2 and MgO particles are marked with red and green arrows in the images, respectively. **c,** TGA analysis of dried pristine samples (SiO_2 and

$Mg(OH)_2$) and samples at different wet-kneading times (10 min and 48 h). **d,** ^{1}H–^{29}Si CP MAS NMR spectra of WK–10min–dried and WK–48h–dried before and after calcination. **e,** 1D ^{25}Mg direct excitation MAS NMR spectra for MgO, WK–10min–calc, and WK–48h–calc, **f,** 2D ^{25}Mg 3Q MAS spectra for MgO (black line) and WK–48h–calc (blue line).

Catalytic performance of catalysts at different wet-kneading times. Figs. 4a and 4b show the activity of wet-kneaded silica–magnesia catalysts obtained after different wet-kneading times. Although the reaction mechanism of the Lebedev process is under discussion,[4,8,61–63] the most plausible mechanism is butadiene formation via acetaldehyde:[2,4,5] (i) ethanol dehydrogenation to acetaldehyde, (ii) aldol condensation between two acetaldehyde forms of 3–hydroxybutanal (acetaldol), (iii, iv) subsequent dehydration and hydrogenation yields crotonaldehyde and crotyl alcohol, respectively, and finally, (v) butadiene formation via intramolecular dehydration. A physical mixture of pristine SiO_2 and MgO catalyst showed limited catalytic performance not only in ethanol conversion (13%), but also in selectivity toward butadiene ($S_{butadiene} = 1.5\%$) (Fig. 4a), in agreement with previous results[15,18]. While butadiene selectivity is low, acetaldehyde selectivity is high (78%), showing that the physical mixing of pristine SiO_2 and MgO is capable to an extent for the initial dehydrogenation step, but cannot provide the appropriate active sites for the entire butadiene pathway. Notably, already after 10 min of wet-kneading, a silica–magnesia catalyst results in substantial increase not only in ethanol conversion (51%), but also in butadiene selectivity (23%). Cross-deposition thus allows for the interplay of acidic and basic sites needed for the multiple reaction steps toward butadiene from ethanol.[13,16,64]

Meanwhile, the catalyst transformations occurring during wet-kneading are not necessarily beneficial for the Lebedev process (Fig. 4a). For example, ethanol conversion gradually decreases by 20% after 72 h of wet-kneading and ethylene selectivity increases, which is an unwanted byproduct. This detrimental effect of prolonged wet-kneading on efficiency in the Lebedev process was not expected, as more magnesium silicates are formed and dispersed over the catalyst surface by extended dissolution/cross-deposition compared with shorter wet-kneading (Supplementary Fig. 11); therefore, more ethanol should be converted to butadiene over these magnesium silicates. A textural effect is ruled out as the Brunauer–Emmett–Teller (BET) specific surface area of wet-kneaded catalysts at different wet-kneading times remains nearly unaltered (Supplementary Fig. 12).

The balanced acidic and basic sites have been often proposed as a key to obtain higher yield of butadiene.[3,4,66,7,13,16–18,21,25,65] For example, in the two-step ethanol-to-butadiene process on zeolite beta catalysts, a dependency was observed between the amount ratio of acidic and basic sites and butadiene selectivity (the highest butadiene selectivity at the acid/base ratio of ~1.2).[67] We characterized the wet-kneaded silica–magnesia catalysts using a temperature-programmed desorption (TPD) using ammonia and carbon dioxide as probe molecules to determine the number of acidic and basic sites of the catalysts, respectively, (Supplementary Fig. 13). The acidity–basicity characterization results show a "general" trend in ethanol conversion, *i.e.*, the catalysts with an acid/base amount ratio around 2 show high ethanol conversion, whereas those with a ratio higher than 4 give low ethanol conversion. However, this analysis does not provide a clear picture of the role of the acidic and basic sites of wet-kneaded silica–magnesia catalysts in the Lebedev process and corresponding butadiene selectivity. A recent study from Szabo et al. also reflects the difficulty in determining a clear relationship between acid–base sites and catalytic performance in the Lebedev process.[68] All these results suggest that not all the magnesium silicates are beneficial for butadiene production and/or the spatial distribution of those active sites is not adequate to carry out the multi-step catalytic reaction.

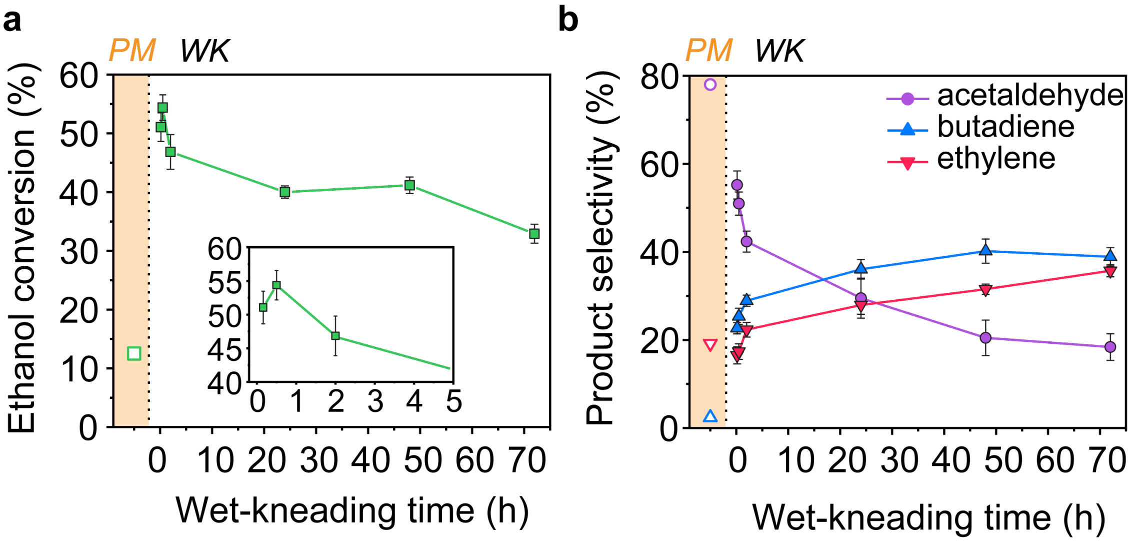

Figure 4 | Catalytic testing results of wet-kneaded silica–magnesia catalysts at different wet-kneading times. Catalytic performance of a catalyst prepared by physical mixing of SiO_2 and $Mg(OH)_2$ (PM) is included for comparison. **a**, Ethanol conversion and **b,** product selectivity. All samples were dried and calcined before the reaction test.

Rational design of two model components in wet-kneaded catalysts. As seen above, wet-kneading generates active sites by providing an environment for simultaneous dissolution/cross-deposition of Si and Mg, to ultimately give a mixture of two particles with the contrasting catalyst surfaces (*e.g.*, Mg on SiO_2 and Si on MgO). These heterogeneous features inherent in the traditional wet-kneaded silica–magnesia catalysts hamper the establishment of direct structure–performance relationships for the Lebedev process. To disentangle these contributions, we modified the traditional wet-kneading method and prepared two model catalysts wherein either SiO_2 or MgO are selectively decorated with Mg and Si (Mg/SiO_2 and Si/MgO), respectively (Fig. 5a). The materials were prepared either in ammonium nitrate or ammonium hydroxide solutions, which provide wet-kneading medium pH values of 8.3 or 11.4, respectively. At a pH of 8.3, the dissolution of SiO_2 is limited,[53,69] whereas the solubility of magnesium species is greatly enhanced by $>10^{14}$ with respect to pure $Mg(OH)_2$ owing to the formation of magnesium nitrate ($K_{sp,Mg(NO_3)_2}$ and $K_{sp,Mg(OH)_2} = 2.4 \times 10^3$ and 5.6×10^{-12},[70] respectively). In contrast, SiO_2 nanoparticles can be completely dissolved at a pH of 11.4 (~10 times solubility increase compared to a pH of 7),[71,72] while $Mg(OH)_2$ retains its morphological structure.

HAADF–STEM with EDX analysis confirmed the disentanglement of two constituents: neither SiO_2 nor MgO phases observed on the Si/MgO and Mg/SiO_2 model systems, respectively (Fig. 5a and Supplementary Fig. 14). PXRD results support the above observation that pristine SiO_2 and MgO are not present in the corresponding model systems of Si/MgO and Mg/SiO_2, respectively, whereas the wet-kneaded catalyst (WK–72h–calc) showed contributions from both pristine SiO_2 and MgO (Supplementary Fig. 15). The crystallite sizes of MgO in WK–72h–calc and Si/MgO were similar (8.3 and 8.4 nm, respectively), indicating that the modified wet-kneading only alters the surface of MgO by selective Si dissolution/deposition.

Figure 5b highlights the catalytic performances of the two model catalysts with pristine MgO and WK–72h–calc catalysts for comparison. Pristine SiO_2 showed no catalytic activity in the Lebedev process (Supplementary Fig. 16), whereas MgO can produce butadiene with a very low selectivity (3.2%). This indicates that the multiple reaction steps toward butadiene can occur to a limited extent on the intrinsic acidic/basic sites on the MgO surface (Supplementary Fig. 13). Similarly, at a sufficiently low flow rate, Hayashi et al. observed that the butadiene selectivity was comparable for MgO and a metal-promoted phyllosilicate (Zn–talc).[73] Meanwhile, the two model catalysts displayed contrasting catalytic performances, showing the highest selectivity towards ethylene (Mg/SiO_2) and butadiene (Si/MgO) among all catalysts tested in this study (85% and 42%, respectively). This suggests that the cross-deposition of Mg and Si yields two components with both undesired and desired catalytic performance characteristics.

The chemical structure of the species on Mg/SiO_2 and Si/MgO catalysts was investigated using ^{29}Si and ^{25}Mg NMR spectroscopy. Figs. 5c,d show 1D ^{1}H–^{29}Si CP MAS NMR spectra and 2D ^{1}H–^{29}Si heteronuclear correlation spectroscopy (HETCOR) experiments of the two model catalysts together with those of WK–72h–calc for comparison. The results show that a linear combination of the spectra from the two model catalysts closely resembles the spectral features of the traditional wet-kneaded silica–magnesia catalysts. For example, the Mg/SiO_2 catalyst showed ^{29}Si resonances from bulk SiO_2 (Q^3 and Q^4 at −100 and −110 ppm, respectively) with two additional peaks at −84 and −92 ppm, which are attributed to amorphous magnesium silicates (Q^2(1Mg,1OH,2Si) and Q^3(1Mg,3Si), respectively.[53] As seen from the PXRD patterns (Supplementary Fig. 15), the Mg species on SiO_2 surface do not form crystalline-layered magnesium silicates owing to the lack of crystalline octahedral Mg^{2+} layers. Interestingly, the correlations between ^{29}Si and ^{1}H was mostly observed from silanols associated with physisorbed and hydrogen bonded water ($\delta^{1}H \approx 5$ ppm).[74] Owing to the low Mg content in Mg/SiO_2 (2.6 wt% Mg), we used a quadrupolar Carr–Purcell–Meiboom–Gill pulse sequence combined with double–frequency sweeps (DFS–QCPMG) to enhance the ^{25}Mg signal intensity (Supplementary Fig. 17). Notably, Mg/SiO_2 showed a distinct ^{25}Mg resonance with a large quadrupolar constant (C_q = 2.6 MHz at δ_{iso} 15 ppm), indicating that the bonding geometries of the surface Mg species are considerably different from the Mg species in pristine MgO and those in the Si/MgO catalyst. The acid/base properties of the Mg/SiO_2 catalyst show a remarkable increase in the number of acidic sites compared with the original SiO_2 materials (Supplementary Fig. 13), suggesting isolated Mg species on SiO_2 surface retain an acidic nature toward ethylene formation.

Meanwhile, for the Si/MgO catalyst, four ^{29}Si resonances are observed at −77, −85, −93 and −97 ppm with characteristic ^{1}H correlations ($0.5 < \delta^1H < 2$ ppm), attributed to structural hydroxyl groups (Si–OH–Mg) (Figs. 5c,d and Supplementary Fig. 18). Similar ^{1}H chemical shifts were observed for phyllosilicates when the hydroxyl groups were part of octahedral Mg layers but pointing toward the surface Si units.[75] Thus, we assign the resonances observed for the Si/MgO catalyst as hydrous magnesium silicates, *e.g.*, Q^1(3Mg,1Si), Q^2(2Mg,2Si), and lizardite- and talc-type Q^3(1Mg,3Si). The ^{25}Mg 3Q MAS NMR spectrum of the Si/MgO catalyst also suggests that some surface Mg species is decorated with deposited Si species, as also observed for WK–48h–calc (Supplementary Fig. 10 and Supplementary Table 3). The TPD data furthermore shows that in this catalyst, additional acidic sites are created, showing *ca.* 20- and 3-times higher numbers of acidic sites than pristine SiO_2 and MgO, respectively (Supplementary Fig. 13). These results, together with the electron microscopy measurements (Fig. 5a and Supplementary Fig. 14), indicate that new acidic sites are created in close proximity to a matrix of basic MgO sites and this catalytic environment is very selective for the formation of butadiene while impeding the reaction of ethanol to ethylene.

To investigate further the effect of acid/base proximity, the catalytic performance of WK–10min–calc and WK–30min–calc wet-kneaded samples and the Si/MgO sample, showing similar acid/base ratios, were compared. Clearly, the Si/MgO sample show ~20% higher selectivity to butadiene compare to the wet-kneaded samples containing a fraction of their acid and basic sites physically separated. We also performed measurements with combination of physical mixtures of Si/MgO and Mg/SiO_2. The results (Supplementary Fig. 16b), clearly show that the physical mixtures are also not able to achieve higher butadiene selectivity. All these results highlight the importance of having acid and basic sites in close proximity for the Lebedev reaction.

Mechanistic investigation by using *operando* DRIFT-MS spectroscopy. Although the ethanol-to-butadiene reaction is generally considered to occur via an acid–base mechanism, there has not been a clear reaction scheme of the catalytic sites. For example, the acid and base sites on wet-kneaded silica–magnesia catalysts have been commonly attributed to unsaturated Mg^{2+} as Lewis acid sites[13,21] and MgO (and/or MgOH) as basic sites,[25,61] whereas other studies report the surface silanol as weak Brønsted acid sites[16,76] and the Si–O–Mg sites as basic sites.[13,76] Based on the two model systems where we can identify the contributions from each component (Mg/SiO_2 and Si/MgO), the structure–performance relationship and the reaction mechanism in the Lebedev process were investigated by *operando* diffuse reflectance infrared Fourier transform spectroscopy coupled with mass spectrometry (DRIFTS–MS). The DRIFTS spectra of the samples are shown in Fig. 5e. For the Mg/SiO_2 catalyst, compared to Si/MgO, the asymmetric CH_3 stretching of ethanol[77] is blue shifted to 2984 cm^{-1} under the reaction condition at 425 °C (Fig. 5e). This suggests that orbital rehybridization of the CH_3 group occurs upon adsorption on the surface of Mg/SiO_2 and the H–C bond (in the CH_3 group) becomes more polarized[78] (*i.e.*, increases the partial positive charge on the H and the negative charge on the C). Thus, we expect that the CH_3 group interacts with the Mg–O–Si surface, where Mg^{2+} acts as a Lewis acid site and stabilizes the carbanion (Supplementary Fig. 19).[61] This can be supported by the *operando* DRIFTS results that interactions between the alcohol functional group and the hydroxyl groups of the catalyst surface are not evidently observed during the reaction (Supplementary Fig. 20). Thus, the dehydration of ethanol to ethylene is highly favored on isolated Mg units on SiO_2 (Fig. 5b), especially in proximity of the acidic (Mg^{2+}) and conjugated base (Mg–O–Si). This is in line with the increased ethylene selectivity observed for catalysts containing more of Mg/SiO_2 component, such as longer wet-kneaded catalysts and the physical mixture of Si/MgO and Mg/SiO_2 (Fig. 4 and Supplementary Fig. 16).

For Si/MgO and WK–72h–calc, which retain a phase of dispersed Si units on MgO, the surface hydroxyl groups of Si/MgO and WK–72h–calc catalysts interact with ethanol and show a negative IR band at ~3730 cm^{-1}, a band completely absent for the Mg/SiO_2 catalyst (Supplementary Fig. 20). This indicates a strong interaction between the terminal Si–OH–Mg groups of the Si/MgO surface (rather than Mg–OH, with an absorption band at 3749 cm^{-1}, see Supplementary Figs. 20, 21 and Supplementary Note 2). Moreover, in the 3600–3200 cm^{-1} region, a broad OH stretching band is observed and is attributed to intermolecular hydrogen bonding of ethanol with the catalyst surface. We expect that the interactions previously observed by DRIFTS studies between the reactants/intermediates and the surface hydroxyl groups on wet-kneaded silica–magnesia catalysts[61,66,76,79] are indeed attributed to the Si/MgO surface (Si–OH–Mg). Notably, an additional IR band is observed at 2730 cm^{-1} (Fig. 5e), which is attributed to the asymmetric stretching of the CH bond at the alpha carbon of the adsorbed ethanol.[79] Taken together with the rapid formation of H_2 on the Si/MgO catalyst (Supplementary Fig. 22), the heterolytic elimination of hydrogen from ethanol is favored[13,80,81] and consequently, acetaldehyde is preferably produced (Supplementary Fig. 19b). Although the attribution of the bands at 1700–1200 cm^{-1} is cumbersome and has been assigned to intermediates (*e.g.*, surface acetates)[66,82–85] or the overlap of several vibration modes of CH_x or OCO(H) species,[79,86,87] the IR feature at 1610 cm^{-1} is clearly observed for Si/MgO (and WK–72h–calc catalysts) and attributed to C=C stretching of key intermediate species such as crotyl alcohol (Fig. 5e).[61,76] For the Mg/SiO_2 model catalyst, these IR features of intermediates towards butadiene are not observed, which is in line with its low butadiene selectivity. We additionally performed a DRIFTS–MS study on pristine MgO and Si/MgO catalysts under temperature–programmed surface reaction (TPSR) conditions (Supplementary Fig. 23). In both cases, we could not observe the characteristic IR bands and MS spectra for crotonaldehyde and crotyl alcohol intermediates due to rapid and subsequent dehydrations to butadiene under reaction conditions[85,91]. The spectral features of both samples at 50 °C are similar but with different intensity ratios. At high temperature, the IR bands of acetaldehyde at 3020 and 2793 cm^{-1} (CH_3 and CH stretching, respectively)[66] are more predominant on the MgO surface compared to Si/MgO. This suggests that acetaldehydes are strongly adsorbed and stabilized on the Mg^{2+}–O^{2-} pair in the horizontal configuration,[92,93] making the subsequent reactions toward butadiene facing difficulty to occur as MgO lack acidic sites for aldol condensation reactions. Since this strong adsorption of acetaldehyde is not observed for the Si/MgO catalyst, we propose that Si incorporation in the MgO domain could reduce the affinity of the intermediates on the catalyst surface and/or enable the subsequent reactions to butadiene (e.g., aldol condensation, dehydrations of acetaldol and crotyl alcohol) by the cooperative interplay of acidic Si species in the basic MgO domain with contributions from neighboring hydroxyl groups (Si–OH–Mg). This again highlights that the catalytic sites for the ethanol-to-butadiene pathway cannot be provided by individual acidic and basic sites (and their physical mixtures (Fig. 4) but can be remarkably promoted by the acid–base sites in close proximity, created via wet-kneading.

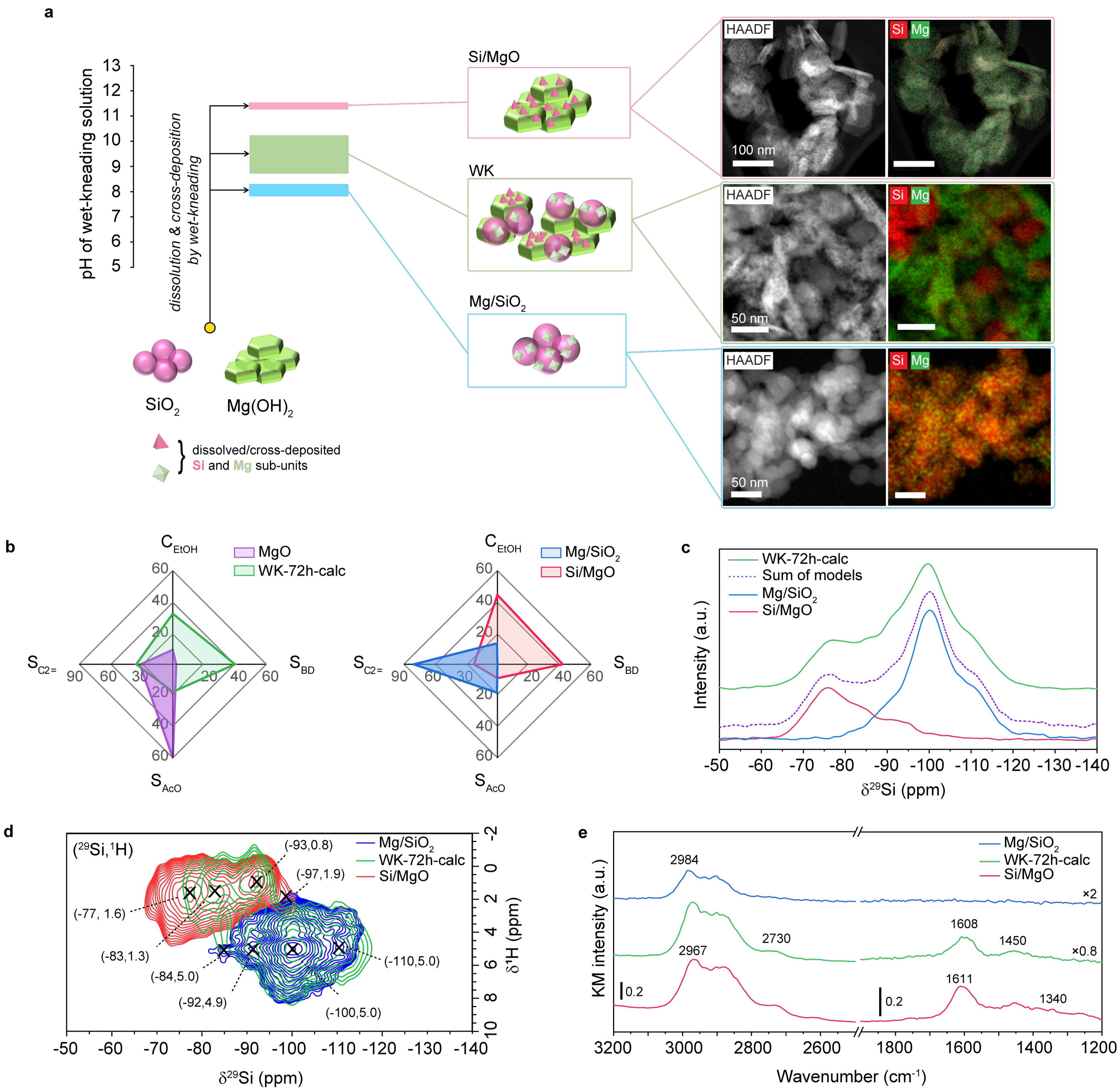

Figure 5 | Identification of key surface magnesium silicates responsible for the one-step Lebedev process. a, Scheme for the preparation of model catalysts using modified wet-kneading. HAADF–STEM and EDX images of calcined catalysts are included in the inset. **b,** Catalytic activity testing results of two model catalysts compared with MgO and wet-kneaded silica–magnesia (WK–72h–calc) catalysts. The reactants and products are denoted as ethanol (EtOH), ethylene (C2=), acetaldehyde (AcO), and butadiene (BD). **c,** 1D ^{1}H–^{29}Si CP MAS NMR and **d,** 2D ^{1}H–^{29}Si CP FSLG–HETCOR spectra of WK–72h–calc, and Si/MgO and Mg/SiO$_2$ catalysts. **e,** *Operando* DRIFTS spectra acquired during continuous ethanol dosing on the catalysts at 425 °C. Intensities of the NMR and DRIFTS spectra are processed for clarity.

Conclusions and outlook

Wet-kneading is a rather non-conventional catalyst synthesis method, but essential for the preparation of active silica-magnesia catalysts for the one-step ethanol-to-butadiene process. The chemical changes that this preparation method elicits in pristine SiO_2 and $Mg(OH)_2$ precursors, in particular the nature of the magnesium silicates thought to be the active components, has long been unclear. We demonstrated that under wet-kneading conditions, the cross-deposition of Si and Mg species on $Mg(OH)_2$ and SiO_2, respectively. Two model catalysts prepared by modified wet-kneading, *i.e.*, Si/MgO and Mg/SiO_2, serve different catalytic roles in the Lebedev process. More specifically, it has become evident that the magnesium silicates on Si/MgO can be held responsible for butadiene formation, while the magnesium silicates on the Mg/SiO_2 primarily produce ethylene. The close proximity of acidic and basic sites in Si-OH-Mg species is thought to be key to efficient conversion, by lowering the activation energy of multiple steps toward butadiene. The insights provided here on the structural requirements for wet-kneaded silica–magnesia catalysts will aid in the development of next-generation Lebedev catalysts.

Methods

Catalyst synthesis. The wet-kneaded silica–magnesia catalysts were prepared from Stöber SiO_2 and $Mg(OH)_2$ precursors according to published procedure.[17,21] The Stöber SiO_2 was prepared by hydrolysis of tetraethyl orthosilicate in a mixture of ethanol and ammonium hydroxide solution. After 15 h of aging, solid SiO_2 nanoparticles were obtained using a rotary evaporator at reduced pressure. The $Mg(OH)_2$ was synthesized by adding 0.4 M NaOH aqueous solution dropwise to 0.2 M $Mg(NO_3)_2$ aqueous solution until the pH reached 12. The precipitated $Mg(OH)_2$ particles were separated by centrifugation and washed multiple times with deionized water. The as-made wet-kneading precursors were dried overnight in a convection oven at 120°C. The dried precursors were then wet-kneaded in deionized water (the nominal molar ratio of Si and Mg was 1.0 and the mass ratio of liquid to solid was 95.7 g/g) at room temperature while varying wet-kneading time (10 min to 72 h). After wet-kneading, the samples were obtained by centrifugation and dried overnight at 120°C (named WK-*time*-dried, where *time* = 10 min to 72 h). Samples obtained after the drying were finally calcined at 500°C for 5 h with a heating rate of 5°C min^{-1} (denoted as WK-*time*-calc). For the two model catalysts (Mg/SiO_2 and Si/MgO), modified wet-kneading was performed for 72 h in 3 M ammonium nitrate and 7.3 M ammonium hydroxide aqueous solutions, respectively. The model catalysts were obtained by centrifugation, dried and calcined as described above. The loading of Mg and Si on SiO_2 and MgO were 2.6 and 9.8 wt.%, respectively (determined by ICP–OES analysis). The pH of the wet-kneading medium was measured using a Mettler Toledo SevenMulti with an InLab®Expert PRO–ISM electrode.

Inductive coupled plasma optical emission spectroscopy (ICP–OES). Elemental analysis for Si and Mg was conducted on a 5100 ICP–OES instrument using argon as the carrier gas. Digestion was executed with a solution containing a mixture of hydrochloric acid, nitric acid and hydrofluoric acid (6:2:1 v/v ratio) at max settings of 273°C and 35 bar on an UltraWAVE apparatus (Milestone).

Scanning transmission electron microscopy combined with energy dispersive X-ray spectroscopy. High-angle annular dark-field scanning transmission electron microscopy (HAADF–STEM) analysis and energy dispersive X-ray (EDX) elemental mapping of the samples were carried out with an FEI Titan G 2 80–300 kV electron microscope operated at 300 kV. Elemental maps were acquired with an electron beam current of 0.5 nA and an average time per single map of ~1 min. Quantitative EDX area mappings were calculated with 75 lines that consist of 25 pixels per line.

Thermal gravimetric analysis (TGA). TGA measurements were performed using a Mettler Toledo TGA/DSC1 Star^e System with a sample mass of ~15 mg. The heating program was set as same as the calcination step under continuous air flow of 20 ml min^{-1}.

Powder X-ray diffraction (PXRD). PXRD patterns were acquired on a Bruker D8 Advance operated at 40 kV and 40 mA using monochromatic Cu Kα ($\lambda = 1.5406$ Å) radiation, while applying a scan speed of 8 sec step^{-1} and a step size of 0.03° over a 2θ range of 5°–80°. Crystalline phase identifications was conducted in Diffract.Eva software with the help of the PDF–4+ (2019) crystal database. The crystallite size of the catalysts was calculated using the Scherrer equation with a shape factor of 0.89 and an instrument width of 0.05. The best match of experimental patterns was observed with brucite ($Mg(OH)_2$) crystal phase exhibiting hexagonal settings and crystallizing in the P–3m1 (#164) space group with unit cell parameters $a = b = 3.1477$ Å, $c = 4.7717$ Å, $\alpha = \beta = 90°$, and $\gamma = 120°$. Pawley refinements were performed using brucite ($Mg(OH)_2$) crystal data[94] with the help of Reflex from the Accelrys Material Studio software package. During the refinements, the unit cell parameters were adjusted, and the background and peak shape were modeled by a four-term polynomial and Pearson VII function, respectively. Other textural characteristics such as degree of crystallinity were also analyzed in Reflex (Accelrys) over the full measured range. Because the brucite has a lamellar structure with interlamellar distances coinciding with the *c*–axis, the (001) diffraction line was taken into evaluation when analyzing expansion/contraction in staking spaces between $[Mg(OH)_2]_n$ sheets.

Nitrogen and argon physisorption. N_2 physisorption was measured at –196°C using a Micromeritics ASAP 2420 high-throughput analysis system. Samples were outgassed at 300°C under vacuum for 8 h. The specific surface areas were estimated according to the Brunauer–Emmett–Teller (BET) method in the relative pressure range (p/p_0) of 0.05–0.95. Ar physisorption was performed at –186°C using a Micromeritics ASAP 2040 with micropore option. Prior to the physisorption experiment, the samples were dried overnight at 350°C under vacuum ($p < 2$ µmHg) for 4 h and additionally 2 h at 90°C before the start of micropore analysis (10°C min^{-1} ramp rate). During the low-pressure incremental dose mode up to relative pressure of 0.01, samples were dosed with 7 mL g^{-1} adsorptive per gram sample. BET derived surface areas were calculated according to Rouquerol criteria.[95] The microporous area and micropore volume were calculated using the Dubinin–

Radushkevich method (MicroActive v4.00 software from Micromeritics). Pore size distribution was obtained using SAIEUS v3.0 software, while applying a DFT model (Oxide–Ar–87, 2D–nonlocal density functional theory (NLDFT) heterogenous surface) on the adsorption data. For the data fitting, values for lambda were set between 2.5 and 3 and standard deviations of the fits was between 0.75 and 0.98.

Temperature-programmed desorption using ammonia and carbon dioxide as probe molecules. Temperature-programmed desorption of ammonia (NH_3) and carbon dioxide (CO_2) was performed on a Micrometrics ASAP 2920 unit. The samples were pretreated in a quartz reactor at 350 °C for 30 min and cooled to 40 and 50°C in helium (He) flow. Subsequently, ammonia (10 vol.% in He) and CO_2 (99.999%) were introduced to the catalyst for 15 min at 40 and 50°C, respectively. Then, the flow was switched to He for 15 min to remove physisorbed species on the catalyst surface. Finally, the sample was heated to 500°C and 700°C for NH_3 and CO_2, respectively, and the desorption of NH_3 and CO_2 was detected using a thermal conductivity and mass spectrometry detectors.

Diffuse reflectance IR and mass spectroscopy. The DRIFTS–MS study was performed on a Nicolet 6700 FT-IR spectrometer equipped with a liquid nitrogen cooled mercury–cadmium–telluride (MCT) detector combined with an online gas-phase Transpector CPM Mass Spectrometer (1–100 amu). He (>99.999%), which has no overlap with the main products or intermediates in the ethanol conversion, was utilized as the carrier gas. For TPSR experiments, ~40 mg of sample was pretreated at 425°C for 40 min in a He flow (20 ml min^{-1}) with a heating rate of 5°C min^{-1}. The samples were then cooled to 50°C and loaded with ethanol for 30 min using He as the carrier gas. After that, the samples were purged with He for 30 min to eliminate the physically adsorbed ethanol at 50°C. Then, the ethanol TPSR experiment was performed in the range of 50°C –500 °C (held at 500°C for 30 min) with a heating rate of 5°C min^{-1}. For *in situ* DRIFTS experiments, the same pretreatment procedure was adopted without the cooling step, and ethanol was continuously introduced at 425°C. The *in situ* DRIFT spectra were obtained by subtracting the background of bare catalyst after the pretreatment and the information about the gas-phase ethanol was obtained by flowing ethanol to the cell loaded with KBr. The IR data was processed by means of Kubelka–Munk conversion using OMNIC 8 software (version 8.2.0.387) The online gas phase products were analyzed by MS and referred to the database of the National Institute of Standards and Technology (NIST). The m/z values of the reactant and products were referred as follows: hydrogen (2), helium (4), water (17), ethylene (26, 27), ethanol (31), butadiene (39, 54), crotyl alcohol (57), and crotonaldehyde (70). Acetaldehyde is not specified in the MS study due to its complexity with other possible products, such as m/z = 29 (ethyl radical) and 44 (carbon dioxide).

Solid state NMR spectroscopy. For NMR measurements, the samples were ground and transferred to a 4 mm rotor for solid–state NMR experiments. *In situ* ^{29}Si MAS NMR experiments were performed on a Bruker 400 MHz (9.4 T) wide-bore magnet with an AVANCE-III console and equipped with a 4 mm HX probe in double channel ^{1}H, ^{29}Si mode. The experiments were performed at room temperature with magic angle spinning (MAS) frequency of 5 kHz. Note that effective sample temperatures can be 5–10 degrees higher due to frictional heating. Hard ^{29}Si π/2 pulses were applied with a field strength of 125 kHz with 20 s of recycle delay and accumulation of 128 scans. The 1D ^{1}H–^{29}Si CP spectrum was recorded using a 5 s recycle delay, 28 ms acquisition time, and 34560 scans with MAS frequency of 12 kHz. The 2D frequency-switched Lee–Goldberg ^{1}H–^{29}Si HETCOR spectrum was recorded using 4 s recycle delay, 10 ms (F2) and 9.5 ms (F1) acquisition time with accumulation of 1024 scans. During the CP step, ^{1}H CP spin-lock pulses centered at 38 kHz were linearly ramped from 75 to 100% and the ^{29}Si RF field was matched to obtain an optimal signal. ^{1}H and ^{29}Si chemical shifts were referenced externally to adamantane and hexamethyl cyclosiloxane. For DNP–SENS NMR, ~20 mg of sample was prepared by incipient wetness impregnation with 20 µl of 16 mM TEKPol (purchased from Cortecnet) in 1,1,2,2–tetrachloroethane (TCE). TEKPol was dried under high vacuum ($<10^{-4}$ mbar) and TCE was stirred over calcium hydride and distilled *in vacuo*.[96] The DNP–SENS NMR spectra were acquired using 300 GHz/400 MHz Avance III Bruker DNP solid-state NMR spectrometer equipped with a 3.2 mm Bruker triple resonance low-temperature MAS probe. Experiments were performed at ~100 K with 280 GHz gyrotron microwave irradiation. The sweep coil of the main magnetic field was set for microwave irradiation occurring at ^{1}H positive enhancement maximum of the TEKPol biradical. For 1D ^{1}H–^{29}Si DNP–SENS NMR experiments, a 5 s recycle delay, 13 ms acquisition time, and 64 scans with 4 ms contact time at the MAS frequency of 8 kHz were implemented. The DNP enhancement factor (ε) was ~80 for each measurement. The ^{29}Si direct excitation MAS NMR and natural abundance ^{25}Mg NMR were performed on a Bruker 900 MHz (21.1 T) wide-bore magnet. The 1D ^{29}Si direct excitation spectrum was recorded using a 3.2 mm HX probe with 20 s recycle delay at MAS frequency of 20 kHz. The 1D ^{25}Mg direct excitation spectrum was recorded using a 4 mm HX low-gamma probe with 0.5 s recycle delays, 30 ms acquisition time, and accumulations of 1024 scans at MAS frequency of 10 kHz. The 2D ^{25}Mg z-filtered 3Q MAS NMR spectra[97] were recorded using a 0.5 s recycle delay with 7200 scans with 50 µs t1 increments at MAS frequency of 10 kHz. The optimized pulse widths for excitation, conversion and central–transition selective pulses were and 15, 5.3 and 40 µs, respectively. The z-filter delay between the conversion and the selective pulse was 20 µs. Prior to Fourier transformation, the 1D and 2D NMR spectra were processed using an exponential window and a π/3 shifted squared sine-bell window in the F1 dimension, respectively. The 3Q MAS data was processed with a shearing transformation available in Bruker Topspin software (v3.6.3). The Haeberlen convention is used to describe the chemical shift tensor in terms of the isotropic shift ($\delta_{iso} = (\delta_{xx} + \delta_{yy} + \delta_{zz})/\delta_{iso}$) and shift asymmetric parameter ($\eta_{CSA} = (\delta_{yy} - \delta_{xx})/(\delta_{zz} - \delta_{iso})$) with the principal components ordered as $|\delta_{zz} - \delta_{iso}| \geq |\delta_{xx} - \delta_{iso}| \geq |\delta_{yy} - \delta_{iso}|$. The quadrupolar tensor is described by the nuclear quadrupolar coupling constant ($C_Q = eQV_{zz}/h$) and quadrupolar asymmetric parameter ($\eta_Q = (V_{xx} - V_{yy})/V_{zz}$), where e is the electric charge, Q is the nuclear quadrupole moment, and h is Planck's constant. The ^{25}Mg QCPMG, DFS–QCPMG, and ^{1}H–^{25}Mg CP–QCPMG experiments were performed at MAS frequency of 10 kHz or at static condition. Typically, the QCPMG pulse sequence was obtained using a 1 s recycle delay and 40 µs central-transition π refocusing selective pulse with 50 µs of spin-echo delays.[98] During DFS pulse, the DFS pulse the rf frequencies were linearly swept for 4 ms from 300 to 100 kHz. ^{1}H–^{25}Mg CP–QCPMG was performed with 10 ms contact time after optimization using $Mg(OH)_2$. The 1D ^{25}Mg QCPMG, DFS–QCPMG, and CP–QCPMG spectra were apodized using 20 Hz Lorentzian line broadening. The ^{25}Mg 1D DFS–QCPMG and 2D 3Q MAS NMR spectra were fitted using WSolids1 (version 1.21.3) and DMFIT (version dmfit#20200306)[99] software, respectively. ^{25}Mg chemical shifts were externally referenced to $MgCl_3$ at 0 ppm.

Catalytic activity test. All catalytic reactions were conducted in an Avantium four–channel Flowrence XD high–throughput reactor system at 425°C and ambient pressure.[21] The catalyst bed was diluted with silicon carbide to decrease the effect of axial dispersion and to improve heat conduction in the bed. Typically, 50 µL of catalyst was mixed with 200 µL of grit46 silicon carbide and placed in a quartz tube with an internal diameter of 2.3 mm. The liquid hourly space velocity (LHSV, liquid flow volume per hour and per catalyst volume) was $1.0\ h^{-1}$ in nitrogen carrier gas. The unreacted ethanol and reaction products were analyzed by gas chromatography in an Agilent 7890B with three detectors (two flame ionization detectors (FID) and one thermal conductivity detector (TCD)). The FID channels were equipped with a 10 m precolumn with a wax stationary phase and a 30 m Gaspro stationary phase to separate ethanol, acetaldehyde, C1–C7 hydrocarbons and oxygenates. The TCD channel had a PoraPLOT Q GC, a Hayesep Q and a Molsieve for the analytical column. The conversion of ethanol (X) and product selectivities (Si) were calculated based on the following formulas:

$$X = \frac{C_{\mathrm{EtOH}_{in}} - C_{\mathrm{EtOH}_{out}}}{C_{\mathrm{EtOH}_{in}}} \times 100 \tag{1}$$

$$S_i = \frac{i \times C_i}{C_{\mathrm{EtOH}_{in}} - C_{\mathrm{EtOH}_{out}}} \times 100 \tag{2}$$

where $C_{\mathrm{EtOH}in}$ and $C_{\mathrm{EtOH}out}$ are the concentrations determined by GC analysis of ethanol in the blank and in the reactor, respectively. Note that there are no alcohols or any other oxygenates in the detected C4–C7 hydrocarbons.

Acknowledgements

The authors are grateful for the funding support from King Abdullah University of Science and Technology. We thank Dr. Jullian Vittenet and Eganathan Kaliyamoorthy for ICP–OES, Dr. Sergei Lopatin for TEM–EDX measurements, Dr. Chris Canlas for technical support for solid-state NMR spectroscopy, and Klaus Eichele (Universität Tübingen) for WSolids1 software support. Preliminary experiments of this research were performed within the framework of the CatchBio program. The authors gratefully acknowledge the support of the Smart Mix Program of The Netherlands Ministry of Economic Affairs, and the Netherlands Ministry of Education, Culture and Science and NWO (Middelgroot program with grant numberwork of 700.58.102).

Author contributions

S.C. and J.R.M. conceived the research ideas and directed the overall project. S.C. designed the experiments and analyzed the data. T.L. and A.G. collected and processed DRIFTS–MS spectra and catalytic activity test results, respectively. T.S., I.M., G.S., S.T., A.D. E.A.H., X.T., and P.L. characterized the prepared catalysts under guidance of S.C., J.G. and J.R.M. B.S. conducted preliminary experiments for catalyst synthesis under B.M.W. and P.C.A.B. supervision. S.C. and J.R.M. cowrote the paper. All authors discussed the results and commented on different versions of the manuscript.

References

1. Bruijnincx, P. C. A. & Weckhuysen, B. M. Shale Gas Revolution: An Opportunity for the Production of Biobased Chemicals? *Angew. Chemie Int. Ed.* **52**, 11980–11987 (2013).
2. Angelici, C., Weckhuysen, B. M. & Bruijnincx, P. C. A. Chemocatalytic Conversion of Ethanol into Butadiene and Other Bulk Chemicals. *ChemSusChem* **6**, 1595–1614 (2013).
3. Makshina, E. V *et al.* Review of old chemistry and new catalytic advances in the on-purpose synthesis of butadiene. *Chem. Soc. Rev.* **43**, 7917–7953 (2014).
4. Pomalaza, G., Arango Ponton, P., Capron, M. & Dumeignil, F. Ethanol-to-butadiene: the reaction and its catalysts. *Catal. Sci. Technol.* **10**, 4860–4911 (2020).
5. Bin Samsudin, I., Zhang, H., Jaenicke, S. & Chuah, G. K. Recent Advances in Catalysts for the Conversion of Ethanol to Butadiene. *Chem. - An Asian J.* **15**, 4199–4214 (2020).
6. Jones, M. D. Catalytic transformation of ethanol into 1,3-butadiene. *Chem. Cent. J.* **8**, 53 (2014).
7. Pomalaza, G., Capron, M., Ordomsky, V. & Dumeignil, F. Recent Breakthroughs in the Conversion of Ethanol to Butadiene. *Catalysts* **6**, 203 (2016).
8. Dussol, D., Cadran, N., Laloue, N., Renaudot, L. & Schweitzer, J.-M. M. New insights of butadiene production from ethanol: Elucidation of concurrent reaction pathways and kinetic study. *Chem. Eng. J.* **391**, 123586 (2020).
9. Li, F. *et al.* Cooperative CO2-to-ethanol conversion via enriched intermediates at molecule–metal catalyst interfaces. *Nat. Catal.* **3**, 75–82 (2020).
10. Wang, X. *et al.* Efficient electrically powered CO2-to-ethanol via suppression of deoxygenation. *Nat. Energy* **5**, 478–486 (2020).
11. Wang, Y. *et al.* Direct Conversion of CO 2 to Ethanol Boosted by Intimacy-Sensitive Multifunctional Catalysts. *ACS Catal.* **11**, 11742–11753 (2021).
12. Cabello González, G. M. *et al.* Ethanol conversion into 1,3-butadiene over a mixed Hf-Zn catalyst: Effect of reaction conditions and water content in ethanol. *Fuel Process. Technol.* **193**, 263–272 (2019).

13. Angelici, C., Velthoen, M. E. Z., Weckhuysen, B. M. & Bruijnincx, P. C. A. Influence of acid–base properties on the Lebedev ethanol-to-butadiene process catalyzed by SiO2 –MgO materials. *Catal. Sci. Technol.* **5**, 2869–2879 (2015).

14. Natta, G. & Rigamonti, R. Studio roentgenografico e chimico dei catalizzatori usati per la produzione del butadiene dall'alcool. *Chim. Ind.* **29**, 239–243 (1947).

15. Kvisle, S., Aguero, A. & Sneeden, R. P. A. Transformation of ethanol into 1,3-butadiene over magnesium oxide/silica catalysts. *Appl. Catal.* **43**, 117–131 (1988).

16. Janssens, W. *et al.* Ternary Ag/MgO-SiO2 Catalysts for the Conversion of Ethanol into Butadiene. *ChemSusChem* **8**, 994–1008 (2015).

17. Chung, S.-H. *et al.* Role of Magnesium Silicates in Wet-Kneaded Silica–Magnesia Catalysts for the Lebedev Ethanol-to-Butadiene Process. *ACS Catal.* **6**, 4034–4045 (2016).

18. Angelici, C., Velthoen, M. E. Z., Weckhuysen, B. M. & Bruijnincx, P. C. A. Effect of preparation method and CuO promotion in the conversion of ethanol into 1,3-butadiene over SiO2-MgO catalysts. *ChemSusChem* 1–12 (2014) doi:10.1002/cssc.201402361.

19. Li, S. *et al.* Morphological control of inverted MgO-SiO2 composite catalysts for efficient conversion of ethanol to 1,3-butadiene. *Appl. Catal. A Gen.* **577**, 1–9 (2019).

20. Huang, X., Men, Y., Wang, J., An, W. & Wang, Y. Highly active and selective binary MgO–SiO2 catalysts for the production of 1,3-butadiene from ethanol. *Catal. Sci. Technol.* **7**, 168–180 (2017).

21. Chung, S. *et al.* The Importance of Thermal Treatment on Wet-Kneaded Silica–Magnesia Catalyst and Lebedev Ethanol-to-Butadiene Process. *Nanomaterials* **11**, 579 (2021).

22. Yi, H. *et al.* A novel method for surface wettability modification of talc through thermal treatment. *Appl. Clay Sci.* **176**, 21–28 (2019).

23. Lewandowski, M. *et al.* Investigations into the conversion of ethanol to 1,3-butadiene using MgO:SiO2 supported catalysts. *Catal. Commun.* **49**, 25–28 (2014).

24. Taifan, W. E., Bučko, T. & Baltrusaitis, J. Catalytic conversion of ethanol to 1,3-butadiene on MgO: A comprehensive mechanism elucidation using DFT calculations. *J. Catal.* **346**, 78–91 (2017).

25. Taifan, W. E. & Baltrusaitis, J. In Situ Spectroscopic Insights on the Molecular Structure of the MgO/SiO2 Catalytic Active Sites during Ethanol Conversion to 1,3-Butadiene. *J. Phys. Chem. C* **122**, 20894–20906 (2018).

26. Zhang, T., Cheeseman, C. R. & Vandeperre, L. J. Development of low pH cement systems forming magnesium silicate hydrate (M-S-H). *Cem. Concr. Res.* **41**, 439–442 (2011).

27. Tonelli, M. *et al.* Structural characterization of magnesium silicate hydrate: towards the design of eco-sustainable cements. *Dalt. Trans.* 3294–3304 (2016) doi:10.1039/C5DT03545G.

28. Nied, D., Enemark-Rasmussen, K., L'Hopital, E., Skibsted, J. & Lothenbach, B. Properties of magnesium silicate hydrates (M-S-H). *Cem. Concr. Res.* **79**, 323–332 (2016).

29. COLE, W. F. A Crystalline Hydrated Magnesium Silicate formed in the Breakdown of a Concrete

Sea-wall. *Nature* **171**, 354–355 (1953).

30. Roosz, C. *et al.* Crystal structure of magnesium silicate hydrates (M-S-H): The relation with 2:1 Mg-Si phyllosilicates. *Cem. Concr. Res.* **73**, 228–237 (2015).
31. Sindorf, D. & Maciel, G. Cross-polarization magic-angle-spinning silicon-29 nuclear magnetic resonance study of silica gel using trimethylsilane bonding as a probe of surface geometry and. *J. Phys. Chem.* **86**, 5208–5219 (1982).
32. Leonardelli, S., Facchini, L., Fretigny, C., Tougne, P. & Legrand, A. P. Silicon-29 NMR study of silica. *J. Am. Chem. Soc.* **114**, 6412–6418 (1992).
33. Kobayashi, T., Perras, F. A., Slowing, I. I., Sadow, A. D. & Pruski, M. Dynamic Nuclear Polarization Solid-State NMR in Heterogeneous Catalysis Research. *ACS Catal.* **5**, 7055–7062 (2015).
34. Magi, M., Lippmaa, E., Samoson, A., Engelhardt, G. & Grimmer, a. R. Solid-state high-resolution silicon-29 chemical shifts in silicates. *J. Phys. Chem.* **88**, 1518–1522 (1984).
35. Moravetski, V., Hill, J.-R., Eichler, U., Cheetham, A. K. & Sauer, J. 29 Si NMR Chemical Shifts of Silicate Species: Ab Initio Study of Environment and Structure Effects. *J. Am. Chem. Soc.* **118**, 13015–13020 (1996).
36. Pustovgar, E. *et al.* Understanding silicate hydration from quantitative analyses of hydrating tricalcium silicates. *Nat. Commun.* **7**, 10952 (2016).
37. Szabó, B. *et al.* MgO−SiO2 Catalysts for the Ethanol to Butadiene Reaction: The Effect of Lewis Acid Promoters. *ChemCatChem* **12**, 5686–5696 (2020).
38. Walling, S. A., Kinoshita, H., Bernal, S. A., Collier, N. C. & Provis, J. L. Structure and properties of binder gels formed in the system Mg(OH)2–SiO2–H2O for immobilisation of Magnox sludge. *Dalt. Trans.* **44**, 8126–8137 (2015).
39. Bernard, E. *et al.* Characterization of magnesium silicate hydrate (M-S-H). *Cem. Concr. Res.* **116**, 309–330 (2019).
40. Salomão, R., Arruda, C. C. & Antunes, M. L. P. Synthesis, Dehydroxylation and Sintering of Porous Mg(OH)2-MgO Clusters: Evolution of Microstructure and Physical Properties. *Interceram - Int. Ceram. Rev.* **69**, 52–62 (2020).
41. van Aken, P. A. & Langenhorst, F. Nanocrystalline, porous periclase aggregates as product of brucite dehydration. *Eur. J. Mineral.* **13**, 329–341 (2001).
42. Gomez-Villalba, L. S., Sierra-Fernandez, A., Rabanal, M. E. & Fort, R. TEM-HRTEM study on the dehydration process of nanostructured Mg-Ca hydroxide into Mg-Ca oxide. *Ceram. Int.* **42**, 9455–9466 (2016).
43. Rollinson, H. & Adetunji, J. Ionic Radii. in *Encyclopedia of Geochemistry: A Comprehensive Reference Source on the Chemistry of the Earth* (ed. White, W. M.) 738–743 (Springer International Publishing, 2018). doi:10.1007/978-3-319-39312-4_340.
44. Shannon, R. D. Revised effective ionic radii and systematic studies of interatomic distances in halides

and chalcogenides. *Acta Crystallogr. Sect. A* **32**, 751–767 (1976).

45. Green, J. Calcination of precipitated Mg(OH)2 to active MgO in the production of refractory and chemical grade MgO. *J. Mater. Sci.* **18**, 637–651 (1983).
46. Litasov, K. D. & Ohtani, E. Effect of water on the phase relations in Earth's mantle and deep water cycle. in *Advances in High-Pressure Mineralogy* vol. 421 115–156 (Geological Society of America, 2007).
47. Lippmaa, E., Mägi, M., Samoson, a., Engelhardt, G. & Grimmer, a. R. Structural studies of silicates by solid-state high-resolution 29Si NMR. *J. Am. Chem. Soc.* **102**, 4889–4893 (1980).
48. MacKenzie, K. J. D., Bradley, S., Hanna, J. V. & Smith, M. E. Magnesium analogues of aluminosilicate inorganic polymers (geopolymers) from magnesium minerals. *J. Mater. Sci.* **48**, 1787–1793 (2013).
49. Chabrol, K. *et al.* Functionalization of synthetic talc-like phyllosilicates by alkoxyorganosilane grafting. *J. Mater. Chem.* **20**, 9695 (2010).
50. Mackenzie, K. J. D. & Meinhold, R. H. Thermal reactions of chrysotile revisited: a 29Si and 25Mg MAS NMR study. *Am. Mineral.* **79**, 43–50 (1994).
51. Stebbins, J. F., Smyth, J. R., Panero, W. R. & Frost, D. J. Forsterite, hydrous and anhydrous wadsleyite and ringwoodite (Mg 2SiO4): 29Si NMR results for chemical shift anisotropy, spin-lattice relaxation, and mechanism of hydration. *Am. Mineral.* **94**, 905–915 (2009).
52. Temuujin, J., Okada, K. & MacKenzie, K. J. D. Role of Water in the Mechanochemical Reactions of MgO–SiO2 Systems. *J. Solid State Chem.* **138**, 169–177 (1998).
53. d'Espinose de la Caillerie, J.-B., Kermarec, M. & Clause, O. 29Si NMR Observation of an Amorphous Magnesium Silicate Formed during Impregnation of Silica with Mg(II) in Aqueous Solution. *J. Phys. Chem.* **99**, 17273–17281 (1995).
54. Hartman, J. S. & Millard, R. L. Gel synthesis of magnesium silicates: A 29Si magic angle spinning NMR study. *Phys. Chem. Miner.* **17**, 1–8 (1990).
55. Benhelal, E. *et al.* Insights into chemical stability of Mg-silicates and silica in aqueous systems using 25Mg and 29Si solid-state MAS NMR spectroscopy: Applications for CO2 capture and utilisation. *Chem. Eng. J.* **420**, 127656 (2021).
56. Freitas, J. C. C. & Smith, M. E. Recent Advances in Solid-State 25Mg NMR Spectroscopy. in *Annual Reports on NMR Spectroscopy* vol. 75 25–114 (2012).
57. Pallister, P. J., Moudrakovski, I. L. & Ripmeester, J. A. Mg-25 ultra-high field solid state NMR spectroscopy and first principles calculations of magnesium compounds. *Phys. Chem. Chem. Phys.* **11**, 11487–11500 (2009).
58. Blanc, F., Middlemiss, D. S., Gan, Z. & Grey, C. P. Defects in doped LaGaO3 anionic conductors: Linking NMR spectral features, local environments, and defect thermodynamics. *J. Am. Chem. Soc.* **133**, 17662–17672 (2011).

59. Jäger, C., Kunath, G., Losso, P. & Scheler, G. Determination of distributions of the quadrupole interaction in amorphous solids by 27Al satellite transition spectroscopy. *Solid State Nucl. Magn. Reson.* **2**, 73–82 (1993).
60. Hatakeyama, M., Nemoto, T., Kanehashi, K. & Saito, K. Natural abundance solid-state 25Mg MQMAS NMR studies on inorganic solids at a high magnetic field of 16.4 T. *Chem. Lett.* **34**, 864–865 (2005).
61. Chieregato, A. *et al.* On the chemistry of ethanol on basic oxides: Revising mechanisms and intermediates in the lebedev and guerbet reactions. *ChemSusChem* **8**, 377–388 (2015).
62. Sushkevich, V. L. & Ivanova, I. I. Mechanistic study of ethanol conversion into butadiene over silver promoted zirconia catalysts. *Appl. Catal. B Environ.* **215**, 36–49 (2017).
63. Gruver, V., Sun, A. & Fripiat, J. J. Catalytic properties of aluminated sepiolite in ethanol conversion. *Catal. Letters* **34**, 359–364 (1995).
64. Velasquez Ochoa, J., Malmusi, A., Recchi, C. & Cavani, F. Understanding the role of Gallium as a new promoter of MgO-SiO2 catalysts for the conversion of Ethanol into Butadiene. *ChemCatChem* 1–9 (2017) doi:10.1002/cctc.201601630.
65. Taifan, W. E. Catalytic Transformation of Ethanol to 1 , 3-Butadiene over MgO / SiO2 Catalyst Catalytic Transformation of Ethanol to 1 , 3-Butadiene over MgO / SiO 2 Catalyst by. (2018).
66. Taifan, W. E., Yan, G. X. & Baltrusaitis, J. Surface chemistry of MgO/SiO 2 catalyst during the ethanol catalytic conversion to 1,3-butadiene: in-situ DRIFTS and DFT study. *Catal. Sci. Technol.* **7**, 4648–4668 (2017).
67. Klein, A., Keisers, K. & Palkovits, R. Formation of 1,3-butadiene from ethanol in a two-step process using modified zeolite-β catalysts. *Appl. Catal. A Gen.* **514**, 192–202 (2016).
68. Szabó, B. *et al.* Conversion of ethanol to butadiene over mesoporous In2O3-promoted MgO-SiO2 catalysts. *Mol. Catal.* **491**, 110984 (2020).
69. Karkanas, P., Bar-Yosef, O., Goldberg, P. & Weiner, S. Diagenesis in Prehistoric Caves: the Use of Minerals that Form In Situ to Assess the Completeness of the Archaeological Record. *J. Archaeol. Sci.* **27**, 915–929 (2000).
70. Lide, D. R. & Haynes, W. M. 'Mickey'. CRC Handbook of chemistry and physics: a ready-reference book of chemical and physical data: 2009-2010 . (2009).
71. Iler, R. K. & K, I. R. *The Chemistry of Silica: Solubility, Polymerization, Colloid and Surface Properties and Biochemistry of Silica*. (Wiley, 1979).
72. Ayral, A. *et al.* Silica membranes - Basic principles. *Period. Polytech. Chem. Eng.* **50**, 67–79 (2006).
73. Hayashi, Y. *et al.* Experimental and computational studies of the roles of MgO and Zn in talc for the selective formation of 1,3-butadiene in the conversion of ethanol. *Phys. Chem. Chem. Phys.* **18**, 25191–25209 (2016).
74. Kim, H. N. & Lee, S. K. Atomic structure and dehydration mechanism of amorphous silica: Insights

from 29Si and 1H solid-state MAS NMR study of SiO2 nanoparticles. *Geochim. Cosmochim. Acta* **120**, 39–64 (2013).

75. Alba, M. D., Becerro, A. I., Castro, M. A. & Perdigón, A. C. High-resolution 1H MAS NMR spectra of 2∶1 phyllosilicates. *Chem. Commun.* 37–38 (2000) doi:10.1039/a906577f.

76. Ochoa, J. V. *et al.* An analysis of the chemical, physical and reactivity features of MgO–SiO 2 catalysts for butadiene synthesis with the Lebedev process. *Green Chem.* **18**, 1653–1663 (2016).

77. Singh, M., Zhou, N., Paul, D. K. & Klabunde, K. J. IR spectral evidence of aldol condensation: Acetaldehyde adsorption over TiO2 surface. *J. Catal.* **260**, 371–379 (2008).

78. Alabugin, I. V., Bresch, S. & dos Passos Gomes, G. Orbital hybridization: a key electronic factor in control of structure and reactivity. *J. Phys. Org. Chem.* **28**, 147–162 (2015).

79. Ochoa, J. V., Malmusi, A., Recchi, C. & Cavani, F. Understanding the Role of Gallium as a Promoter of Magnesium Silicate Catalysts for the Conversion of Ethanol into Butadiene. *ChemCatChem* **9**, 2128–2135 (2017).

80. Tsuchida, T. *et al.* Reaction of ethanol over hydroxyapatite affected by Ca/P ratio of catalyst. *J. Catal.* **259**, 183–189 (2008).

81. Díez, V. K., Apesteguía, C. R. & Di Cosimo, J. I. Acid-base properties and active site requirements for elimination reactions on alkali-promoted MgO catalysts. *Catal. Today* **63**, 53–62 (2000).

82. Idriss, H., Diagne, C., Hindermann, J. P., Kiennemann, A. & Barteau, M. A. Reactions of Acetaldehyde on CeO2 and CeO2-Supported Catalysts. *J. Catal.* **155**, 219–237 (1995).

83. Guil, J. M., Homs, N., Llorca, J. & Ramírez de la Piscina, P. Microcalorimetric and Infrared Studies of Ethanol and Acetaldehyde Adsorption to Investigate the Ethanol Steam Reforming on Supported Cobalt Catalysts. *J. Phys. Chem. B* **109**, 10813–10819 (2005).

84. Chavez Diaz, C. D., Locatelli, S. & Gonzo, E. E. Acetaldehyde adsorption on HZSM-5 studied by infrared spectroscopy. *Zeolites* **12**, 851–857 (1992).

85. Yan, T. *et al.* Mechanistic Insights into One-Step Catalytic Conversion of Ethanol to Butadiene over Bifunctional Zn–Y/Beta Zeolite. *ACS Catal.* **8**, 2760–2773 (2018).

86. Hemelsoet, K. *et al.* Experimental and theoretical IR study of methanol and ethanol conversion over H-SAPO-34. *Catal. Today* **177**, 12–24 (2011).

87. Aronson, M. T., Gorte, R. J. & Farneth, W. E. An infrared spectroscopy study of simple alcohols adsorbed on H-ZSM-5. *J. Catal.* **105**, 455–468 (1987).

88. Müller, P. *et al.* Mechanistic Study on the Lewis Acid Catalyzed Synthesis of 1,3-Butadiene over Ta-BEA Using Modulated Operando DRIFTS-MS. *ACS Catal.* **6**, 6823–6832 (2016).

89. Sushkevich, V. L., Ivanova, I. I., Ordomsky, V. V. & Taarning, E. Design of a Metal-Promoted Oxide Catalyst for the Selective Synthesis of Butadiene from Ethanol. *ChemSusChem* **7**, 2527–2536 (2014).

90. De Baerdemaeker, T. *et al.* Bimetallic Zn and Hf on silica catalysts for the conversion of ethanol to 1,3-butadiene. *ACS Catal.* **5**, 3393–3397 (2015).

91. Sushkevich, V. L., Ivanova, I. I., Ordomsky, V. V. & Taarning, E. Design of a Metal-Promoted Oxide Catalyst for the Selective Synthesis of Butadiene from Ethanol. *ChemSusChem* **7**, 2527–2536 (2014).

92. Fan, D., Dong, X., Yu, Y. & Zhang, M. A DFT study on the aldol condensation reaction on MgO in the process of ethanol to 1,3-butadiene: Understanding the structure-activity relationship. *Phys. Chem. Chem. Phys.* **19**, 25671–25682 (2017).

93. Dong, X., Liu, C., Fan, D., Yu, Y. & Zhang, M. Insight into the effect of promoters (M = Cu, Ag, Zn, Zr) on aldol condensation reaction based on MgO surface in the process of ethanol to 1, 3-butadiene: A comparative DFT study. *Appl. Surf. Sci.* **481**, 576–587 (2019).

94. Černý, R., Valvoda, V. & Chládek, M. Empirical Texture Corrections for Asymmetric Diffraction and Inclined Textures. *J. Appl. Crystallogr.* **28**, 247–253 (1995).

95. Rouquerol, J., Llewellyn, P. & Rouquerol, F. *Is the BET equation applicable to microporous adsorbents? Studies in Surface Science and Catalysis* vol. 160 (Elsevier B.V., 2007).

96. Dutta Chowdhury, A., Yarulina, I., Abou-Hamad, E., Gurinov, A. & Gascon, J. Surface enhanced dynamic nuclear polarization solid-state NMR spectroscopy sheds light on Brønsted–Lewis acid synergy during the zeolite catalyzed methanol-to-hydrocarbon process. *Chem. Sci.* **10**, 8946–8954 (2019).

97. Amoureux, J. P., Fernandez, C. & Steuernagel, S. Z Filtering in MQMAS NMR. *J. Magn. Reson. - Ser. A* **123**, 116–118 (1996).

98. Larsen, F. H., Skibsted, J., Jakobsen, H. J. & Nielsen, N. C. Solid-State QCPMG NMR of Low-γ Quadrupolar Metal Nuclei in Natural Abundance. *J. Am. Chem. Soc.* **122**, 7080–7086 (2000).

99. Massiot, D. *et al.* Modelling one- and two-dimensional solid-state NMR spectra. *Magn. Reson. Chem.* **40**, 70–76 (2002).

Supplementary Files

- SIETB.pdf